

# Ballistic charge transport in twisted bilayer graphene

Hadi Z. Olyaei<sup>1</sup>, Bruno Amorim<sup>2</sup>, Pedro Ribeiro<sup>1,3</sup>, Eduardo V. Castro<sup>3,4</sup>

<sup>1</sup>*CeFEMA, Instituto Superior Técnico, Universidade de Lisboa, Av. Rovisco Pais, 1049-001 Lisboa, Portugal*

<sup>2</sup>*Centro de Física das Universidades do Minho e Porto,*

*Universidade do Minho, Campus de Gualtar, 4710-057 Braga, Portugal*

<sup>3</sup>*Beijing Computational Science Research Center, Beijing 100084, China and*

<sup>4</sup>*Centro de Física das Universidades do Minho e Porto,*

*Departamento de Física e Astronomia, Faculdade de Ciências,*

*Universidade do Porto, 4169-007 Porto, Portugal*

We study conductance across a twisted bilayer graphene coupled to single-layer graphene leads in two setups: a flake of graphene on top of an infinite graphene ribbon and two overlapping semi-infinite graphene ribbons. We find conductance strongly depends on the angle between the two graphene layers and identify three qualitatively different regimes. For large angles ( $\theta \gtrsim 10^\circ$ ) there are strong commensurability effects - for incommensurate angles the low energy conductance approaches that of two disconnected layers, while sharp conductance features correlate with commensurate angles with small unit cells. For intermediate angles ( $3^\circ \lesssim \theta \lesssim 10^\circ$ ), we find a one-to-one correspondence between certain conductance features and the twist-dependent Van Hove singularities arising at low energies, suggesting conductance measurements can be used to determine the twist angle. For small twist angles ( $1^\circ \lesssim \theta \lesssim 3^\circ$ ), commensurate effects seem to be washed out and the conductance becomes a smooth function of the angle. In this regime, conductance can be used to probe the narrow bands, with vanishing conductance regions corresponding to spectral gaps in the density of states, in agreement with recent experimental findings.

## I. INTRODUCTION

Two-dimensional materials have shown to be widely tunable, providing properties-on-demand for electronic and optical applications. At the same time, their relative simplicity and the degree of sample-purity render these materials an ideal playground to study physical phenomena hard to isolate in more complex compounds. The discovery of both correlated insulating phases [1] and superconductivity [2] in twisted bilayer graphene (tBLG) opened up the possibility to further tune 2D heterostructures into strongly correlated phases and promises to shine new light on the interplay between the insulating and superconducting states.

A key underlying feature of tBLG is the sharp decrease of the Fermi velocity, strongly renormalized for small values of the twist angle,  $\theta$ , between the two graphene layers [3]. For  $\theta \lesssim 1^\circ$ , extremely narrow bands appear at low energies, with the Fermi velocity even vanishing at specific - so-called *magic* - angles [4–8]. It is in this regime that unexpected insulating and superconducting states are observed, pointing to electron correlations as key players. This triggered an intense research interest in this system [9–20]. The flat band regime induced by a finite twist has also been explored experimentally in graphene double bilayers [21–23] and trilayers [24, 25], and is also relevant to other two-dimensional materials [26, 27].

The rotation between layers introduces a long-wavelength modulation of the lattice structure called moiré pattern [28]. For small angles, the moiré wavelength is much larger than the carbon-carbon distance, with the ratio growing as  $1/\theta$ . This represents an ad-

ditional difficulty regarding the theoretical description of the system, since a single moiré may contain several thousands of atoms in the low angle regime. While the minimum Wannier-like tight binding parametrization describing the narrow band sector on the moiré scale is still debated [29–34], the original atomic tight binding model remains a faithful description, despite the large unit cells at smaller angles [4, 5, 7, 8, 35, 36].

Transport measurements in tBLG have been crucial to characterize the small angle regime around the neutrality point. *Superlattice*-induced transport gaps, delimiting so-called moiré bands, have been observed in Refs. [9, 37, 38] for tBLG with  $\theta \sim 2^\circ$ , whenever these bands are completely occupied, for a carrier density  $n = +n_S$ , or fully empty,  $n = -n_S$ , where  $2n_S$  is the total charge density of the moiré bands. Close to the first magic angle, for  $\theta \approx 1.1^\circ$ , besides the gaps at  $n = \pm n_S$ , an insulating state was also detected at half-filling,  $n = \pm n_S/2$ , which cannot be explained within the single particle picture [1]. By changing the carrier density around  $n = \pm n_S/2$ , the resistance drops to zero, signaling the transition to a superconducting state for temperatures below  $T \approx 1.0$  K [2, 10]. Conductance measurements also allowed to detect insulating states at the fractional fillings  $n/n_S = 1/4, 3/4$  [10, 11, 20, 39], and for a larger angle,  $\theta \simeq 1.27^\circ$ , after applying pressure [10]. Transport has further been essential to inspect twisted double bilayers [21, 23], to analyze the role of Coulomb screening in both insulating and superconducting phases of tBLG [40], and to demonstrate atomic reconstruction for  $\theta < 1^\circ$  [41].

Despite its experimental relevance, there are comparatively few theoretical works addressing transport in

graphene heterostructures, in particular on twisted bilayer systems. Ref. [42] has addressed the linear transport regime, using the Kubo formalism, finding that a finite concentration of vacancies suppress the conductivity in a wide energy region. Refs. [43, 44] discuss impurity and phonon scattering, with particular emphasis on the temperature dependence of the resistivity. Within the ballistic regime, an earlier work addressed the transport properties of small nanoribbons with a large angle tBLG section [45] highlighting the importance of edge effects. Recently, a wider single layer graphene nanoribbon with a twisted graphene flake on top was studied in Ref. [46]. An interesting orbital magnetic structure has been predicted at finite source-drain voltage applied only to the graphene nanoribbon. This effect is attributed to the presence of counterflow currents first discussed in [4]. Finally, the effect of a spatially inhomogeneous twist angle - twist disorder - on transport has recently been considered in Ref. [47]. However, the ballistic conductance of tBLG as a function of the twist angle had, to our knowledge, not yet been obtained. Nonetheless, given the high quality of the samples and the reported low temperatures, the ballistic regime ought to be considered to make contact with the experimental findings.

In this paper, we provide a thorough study of the ballistic transport properties of tBLG as a function of the twist angle. We find three qualitatively different regimes, characterizing the dependence of the conductance on  $\theta$ , respectively for small, intermediate and large angles. We pay particular attention to the behavior of conductance near commensurate and incommensurate angles. In the large angle regime, the results are shown to be sensitive to commensurability effects. For intermediate angles, conductance features correlate with the position of the van Hove singularities in the density of states (DOS). In the small angle regime, commensurability effects completely disappear. Superlattice induced gaps are clearly resolved, in agreement with experimental findings.

The structure of the paper is as follows: In Sec. II we introduce the model and describe the methodology used to calculate the conductance and the DOS. In Sec. III, representative results of the transmission for the different angle regimes are presented and discussed. Section IV contains a short summary and the conclusions.

## II. MODEL AND METHODS

We consider transport in two setups, shown schematically in Fig. 1. The setup in (a) is denoted  $1 \rightarrow 1$  and consists of a disk of single layer graphene overlaid on a graphene ribbon. The diameter of the disk is the same as the width of the ribbon, and its orientation is chosen so that the two layers define a circularly shaped tBLG region with the desired twist angle. The second setup, (b) denoted  $1 \rightarrow 2$ , consists of two semi-infinite graphene rib-

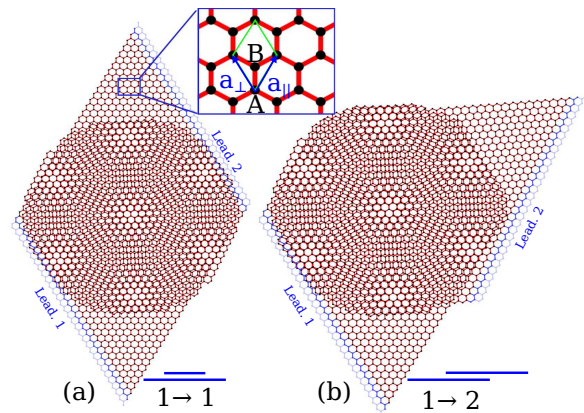


FIG. 1. Twisted bilayer setups used in this work: (a)  $1 \rightarrow 1$  and (b)  $1 \rightarrow 2$  setup. Vanishing blue color denotes the beginning of semi-infinite leads. Lateral views are shown under each setup. The typical linear size of the scattering region is hundred of nanometers.

bons with overlapping ends. Semi-circular edges at the end of each ribbon define an almost circular tBLG region. By adjusting the relative orientation of the ribbons we fix the twist angle. In both setups, the remaining of the monolayer ribbons define semi-infinite leads.

We model  $p_z$  electrons in tBLG through a microscopic tight binding Hamiltonian reading  $H = H_1 + H_2 + H_\perp$ , where  $H_l$ , with  $l = 1, 2$ , is the Hamiltonian for a single layer, and  $H_\perp$  is the interlayer coupling. For the single layer Hamiltonian we write,

$$H_l = -t \sum_{\substack{\mathbf{R}_l, \mathbf{R}'_l \\ |\mathbf{R}_l - \mathbf{R}'_l| \leq a}} c_{l,\alpha}^\dagger(\mathbf{R}_l) c_{l,\beta}(\mathbf{R}'_l), \quad (1)$$

where  $c_{l,\alpha}^\dagger(\mathbf{R}_l)$  creates an electron at the Bravais lattice position  $\mathbf{R}_l$ , of layer  $l$  and sublattice  $\alpha = A, B$ , and the constraint  $|\mathbf{R}_l - \mathbf{R}'_l| \leq a$ , with  $a = 1.42 \text{ \AA}$  for the carbon-carbon bond length, ensures nearest neighbor hopping in each layer. The interlayer coupling is written as  $H_\perp = H_{12} + H_{21}$ , with

$$H_{12} = \sum_{\mathbf{R}_1, \mathbf{R}_2} t_{12}^{\alpha\beta}(\mathbf{R}_1, \mathbf{R}_2) c_{1,\alpha}^\dagger(\mathbf{R}_1) c_{2,\beta}(\mathbf{R}_2), \quad (2)$$

where  $t_{12}^{\alpha\beta}(\mathbf{R}_1, \mathbf{R}_2)$  is the interlayer hopping in the tight binding basis, and  $H_{21}$  obtained from the previous equation by replacing  $1 \leftrightarrow 2$ . To parametrize the interlayer hopping in Eq. (2), we use the two-center approximation and assume  $t_{12}^{\alpha\beta}(\mathbf{R}_1, \mathbf{R}_2)$  depends only on the distance  $r$  between the two  $p_z$ -orbitals,

$$t_{12}^{\alpha\beta}(\mathbf{R}_1, \mathbf{R}_2) \equiv t_{12}^{\alpha\beta}(r),$$

with  $r^2 = d_\parallel^2 + d_\perp^2$  for an interlayer separation  $d_\perp = 3.35 \text{ \AA}$  and an in-plane projected distance  $d_\parallel =$

$|\mathbf{R}_1 + \boldsymbol{\tau}_{1,\alpha} - \mathbf{R}_2 - \boldsymbol{\tau}_{2,\beta}|$  between, where  $\boldsymbol{\tau}_{l,\alpha}$  are the in-plane positions of the orbital centers in the unit cell of each layer. Since the sites in  $A$  and  $B$  sublattices correspond to the same  $p_z$  orbital, we further assume that the interlayer hopping does not depend on the sublattice index,  $t_{12}^{\alpha\beta}(r) \equiv t_{\perp}(r)$ . Using the Slater-Koster parametrization [48], we write

$$t_{\perp}(r) = \cos^2(\gamma) V_{pp\sigma}(r) + \sin^2(\gamma) V_{pp\pi}(r), \quad (3)$$

where the angle  $\gamma$  is such that  $\cos^2(\gamma) = d_{\perp}^2/r^2$ , and following Ref. [49] the spatial dependence of the parameters is given by

$$\begin{aligned} V_{pp\sigma}(r) &= t_{\perp} \exp\left[q_{\sigma}\left(1 - \frac{r}{d_{\perp}}\right)\right], \\ V_{pp\pi}(r) &= -t \exp\left[q_{\pi}\left(1 - \frac{r}{a}\right)\right]. \end{aligned} \quad (4)$$

From the second neighbor intralayer hopping,  $t' = 0.1t$ , we fix  $q_{\pi} = 3.15$ , and assuming  $q_{\pi}/a = q_{\sigma}/d_{\perp}$  yields  $q_{\sigma} = 7.42$  [28]. For the remaining parameters, we consider  $t = 2.79$  eV and  $t_{\perp} = 0.35$  eV. The sum in  $H_{12}$  and  $H_{21}$  is restricted to sites such that the in-plane separation between sites is smaller than a certain cutoff. We have considered only interlayer hopping terms with  $d_{\parallel} < 0.9a$ . Including further distance interlayer hopping terms does not qualitatively alter the description of tBLG [5]. One advantage of the truncation we have chosen is that the first magic angle occurs at a slightly larger value,  $\theta^* \approx 1.6^\circ$ , thus for a slightly smaller moiré cell.

To compute the conductance,  $G$ , we use the Landauer approach. At zero temperature and in the linear regime, the conductance is proportional to the transmission,  $T(\epsilon)$ , for a system with chemical potential  $\epsilon$ . We define  $\bar{T}(\epsilon) = T(\epsilon)/w$ , where  $w$  is the width of the leads, and write the conductance as  $G = G_0 \bar{T}(\epsilon)$ , where  $G_0 = \frac{2e^2}{h}$  is the conductance quantum. For both setups shown in Fig. 1, the circular tBLG region with diameter  $w$  defines the scattering region, which, by construction, is connected to two semi-infinite leads of width  $w$ . We compute the transmission,  $T(\epsilon)$ , from the left lead to the right lead using the Kwant package [50]. Conductance calculations are performed with a scattering region containing around  $\mathcal{N} = 3.77 \times 10^5$  carbon atoms for twist angles  $2^\circ < \theta < 58^\circ$ . For structures with smaller twist angles,  $0 < \theta \leq 2^\circ$  (close to AB stacking) and  $58 \leq \theta < 60^\circ$  (close to AA stacking), larger system sizes were used, with roughly four times the number of carbon atoms, i.e. around  $\mathcal{N} = 1.56 \times 10^6$ . The number of moiré cells in the scattering region ranges from  $\gtrsim 150$  for the smallest angles to several thousands for larger angles. DOS calculations for incommensurate angles are done based on the kernel polynomial method, also provided in Kwant. In this case, the size of the tBLG circular region was

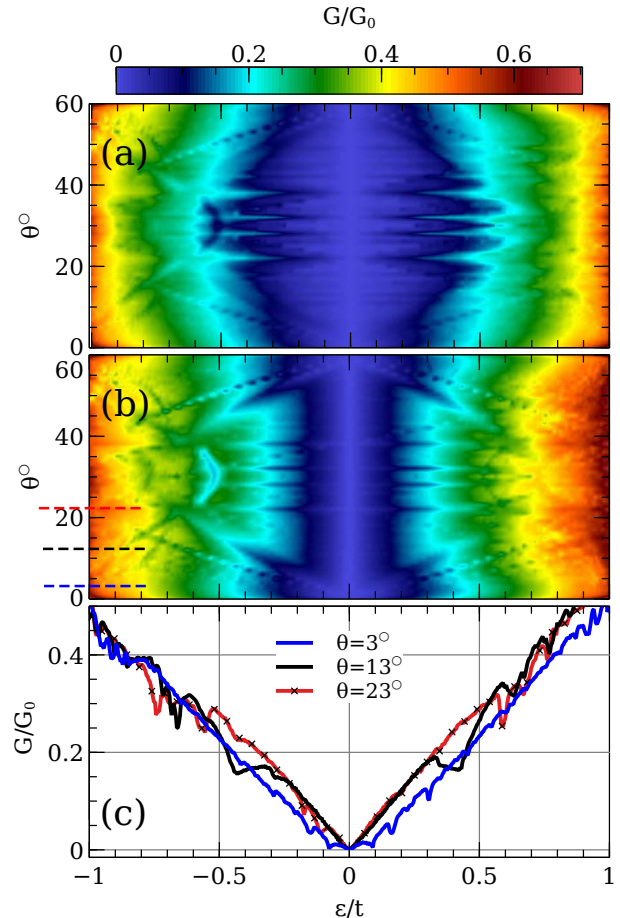


FIG. 2. Density plot of the conductance,  $G$ , as a function of twist angle,  $\theta$ , and energy,  $\epsilon$ , for the two setups considered in this work,  $1 \rightarrow 2$  (a) and  $1 \rightarrow 1$  (b). Panel (c) shows  $G$  vs  $\epsilon$  for three particular angles,  $\theta = 3^\circ$ ,  $13^\circ$  and  $23^\circ$ , depicted as dashed horizontal lines in panel (b).

kept at  $\mathcal{N} = 1.56 \times 10^6$  carbon atoms for angles in the range  $2^\circ < \theta < 58^\circ$ , and  $\mathcal{N} = 4.6 \times 10^6$  carbon atoms for smaller angles,  $0 < \theta \leq 2^\circ$  and  $58 \leq \theta < 60^\circ$ . The DOS and band structures for infinite tBLG systems was also evaluated using a plane wave expansion for (incommensurate structures) and diagonalization of the Bloch Hamiltonian (for commensurate structures).

### III. RESULTS AND DISCUSSION

In this section, we present results for the conductance through a tBLG region as a function of the twist angle for both setups shown in Fig. 1. We start with the analysis of general features regarding the dependence on twist angle, and then move on to discuss in greater detail the three distinct regimes: large, intermediate, and small angles.

### A. General features

The conductance,  $G$ , of tBLG as a function of twist angle,  $\theta$ , for an energy window  $\varepsilon \in [-t, t]$ , is shown in Figs. 2(a) and 2(b) for the two setups  $1 \rightarrow 2$  and  $1 \rightarrow 1$ , respectively. Generally, the conductance is lower at lower energies, increasing non monotonically with energy for both setups, irrespectively of the angle. For  $\theta = 0^\circ$ , we recover AB-stacked bilayer graphene where this general trend has previously been observed [51]. This behavior occurs even if the scattering region is replaced by graphene itself, in which case it is totally determined by the increasing number of channels in the leads, i.e. proportional to the DOS.

In Fig. 2(c) the conductance of the  $1 \rightarrow 1$  setup is shown as a function of energy for three twist angles, representative of the large, intermediate and small twists [corresponding to the three horizontal dashed lines in Fig. 2(b)]. Apart from the general trend of increasing conductance with increasing energy, characteristic features of tBLG for small, intermediate, and large angles can be appreciated. For small angles, the conductance is suppressed within a wider energy region around  $\varepsilon = 0$  when compared with the other two angles. This low energy behavior is associated with the flatband regime in tBLG, and will be further discussed below. Intermediate and large twist angles have similar  $G(\varepsilon)$  at low energies. As will be shown below, at higher energies the intermediate angle case first deviates from the large angle behavior at the characteristic energy of the Von-Hove singularities in tBLG. In the large angle regime, particular features of tBLG are better appreciated as a function of twist angle. A series of peaks and deeps can be seen in Figs. 2(a) and 2(b). As will be discussed below, these features appear at commensurate twist angles with relatively small unit cells.

### B. Large twist angles

For large, incommensurate twist angles and low energies ( $\varepsilon \ll t$ ), the two layers become effectively decoupled: the conductance of the  $1 \rightarrow 1$  setup approaches that of monolayer graphene, while for the  $1 \rightarrow 2$  setup it is strongly suppressed as the electrons need to tunnel to the other layer to conduct. This can be seen in particular for  $\theta = 30^\circ$  in Fig. 3(a), where we also show the graphene conductance as a dashed line for comparison. The low energy decoupling of large angle tBLG has also been obtained with the Kubo formalism within the linear response regime in Ref. [42]. However, at higher energies, deviations from the single layer conductance for the  $1 \rightarrow 1$  setup and an increasing conductance for the  $1 \rightarrow 2$  setup can be seen in Fig. 3(a). This indicates that there is always some remnant coupling even for the largest angles, in agreement with the observations of Ref. [52].

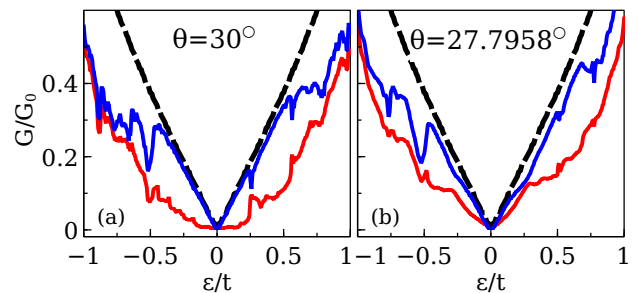


FIG. 3. Conductance,  $G$ , as a function of energy,  $\varepsilon$ , for the  $1 \rightarrow 1$  (blue) and  $1 \rightarrow 2$  (red) setups computed at two large angles: an incommensurate structure with twist angle  $\theta = 30^\circ$  (a) and a commensurate structure with  $\theta \simeq 27.7958^\circ$  (b). The black dashed curve is the conductance of graphene.

The  $\theta = 30^\circ$  tBLG considered above is an example of an incommensurate structure where no true Bravais lattice can be identified, despite the presence of the moiré period. In particular, for the twist angle  $\theta = 30^\circ$ , tBLG has been identified as a new type of quasicrystalline lattice with 12-fold rotational symmetry [53, 54]. For commensurate large angles, however, the conductance of tBLG behaves differently. This can be seen by directly inspecting Fig. 3(b), where we show the conductance  $G(\varepsilon)$  for a commensurate angle close to  $\theta = 30^\circ$ . For the  $1 \rightarrow 1$  setup,  $G(\varepsilon)$  starts to deviate from single layer graphene at lower energies, and for the  $1 \rightarrow 2$  setup, the low energy conductance is not suppressed as for incommensurate angles.

The difference between incommensurate and commensurate structures at large twist angles is better appreciated in Fig. 4(a), where we plot the conductance as a function of twist angle at the fixed energy  $\varepsilon = 0.225t$  (easily reached via back gate field effect). For the  $1 \rightarrow 1$  setup a series of deeps and for the  $1 \rightarrow 2$  setup a series of peaks are clearly seen. These are the same peaks and deeps observed in Figs. 2(a) and 2(b). As shown in Fig. 4(a), the peaks/deeps match perfectly the vertical lines. It is also apparent that the conductance curves are approximately symmetric with respect to the twist angle  $\theta = 30^\circ$ , and for that reason we only plot vertical lines for  $\theta < 30^\circ$ . The vertical lines correspond to a series of commensurate angles, obtained according to the relation

$$\sin\left(\frac{\theta_{mr}}{2}\right) = \frac{r}{2\sqrt{3m^2 + 3mr + r^2}}, \quad (5)$$

where  $m$  and  $r$  are positive coprime numbers [5]. Therefore, the peaks/deeps are conductance signatures of commensurability. They are robust to relative shifts of the layers (pure translations with fixed  $\theta$ ), and in Fig. 4(a) we have averaged over shifts. A few of the largest peaks for the  $1 \rightarrow 2$  setup have been reported also in the incoherent transport regime [55]. In the ballistic regime we see that the structure is very rich, with peaks at many



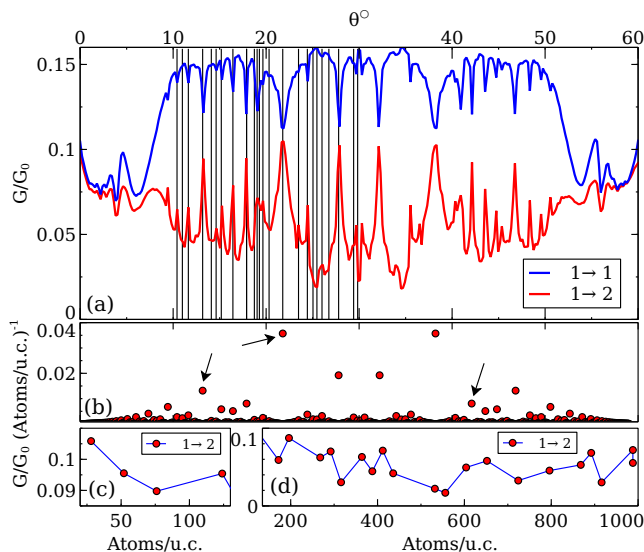


FIG. 4. Conductance,  $G$ , as a function of twist angle,  $\theta$ , for the  $1 \rightarrow 1$  (blue) and  $1 \rightarrow 2$  (red) setups calculated at the energy  $\varepsilon = 0.225t$  (a). The black vertical lines depict the position of commensurate angles, as given by Eq. (5) in the main text. Panel (b) exhibits the inverse of the size of the Wigner-Seitz unit cell for commensurate structures versus the angle. Panels (c-d) show the conductance values of the  $1 \rightarrow 2$  setup for commensurate structures as a function of size of the Wigner-Seitz unit cell for small and large unit cells respectively.

commensurate angles. In fact, we are lead to speculate that peaks (deeps) may be present at every commensurate angle, though its relative height (depth) may hinder the observation of most of them. This is corroborated by an apparent correlation between the height (depth) of the peak (deep) and the size of the Wigner-Seitz unit cell for the corresponding commensurate lattice structure, as shown in Fig. 4(b). There, the inverse of the size of the Wigner-Seitz unit cell, measured in terms of the number of atoms inside the cell, is plotted as a function of the respective commensurate angle. By inspection it can be seen that the higher the conductance peak in Fig. 4(a) for the  $1 \rightarrow 2$  setup (the lower the deep for the  $1 \rightarrow 1$  setup) the smaller the respective Wigner-Seitz unit cell. The six peaks reported in Ref. [55] for the incoherent regime correspond precisely to the six twist angles with smallest Wigner-Seitz unit cell (higher conductance).

The conductance as a function of the size of the Wigner-Seitz unit cell for commensurate structures is shown in Fig. 4(c). In the large angle regime (unit cell sizes  $\lesssim 100$ ), it is clear that the conductance decreases as the size of the cell increases. For intermediate to low angles (unit cell sizes  $\gtrsim 100$ ), this commensurability effect is lost. This agrees with the fact that  $r = 1$  structures, for which the unit cell coincides with the Moiré cell, are special in the small-angle limit and determine the physics of all types of commensurate structures [5]. For very small

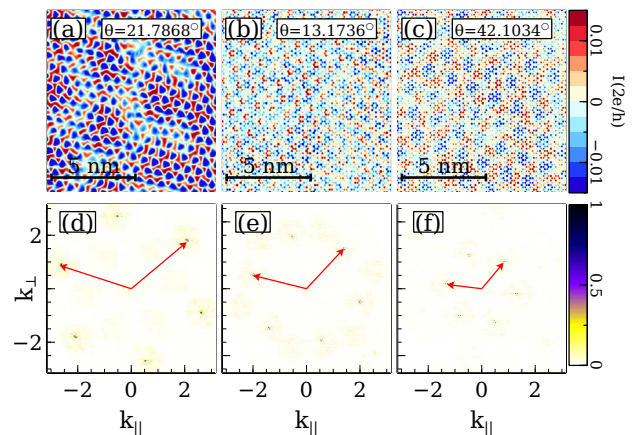


FIG. 5. (a-c) Interlayer current mapped onto the bottom layer as a density plot at  $\varepsilon = 0.225t$  for three commensurate structures. In terms of the integers  $m$  and  $r$  in Eq. (5), ( $m = 1, r = 1$ ) in (a) and in (b), ( $m = 1, r = 4$ ) in (c). (d-f) 2D Fourier transform of the interlayer current shown in (a-c) as a function of  $k_{\parallel}$  and  $k_{\perp}$ , respectively the longitudinal and transverse momenta relative to the direction of the bottom lead ribbon. The arrows are two representative vectors of the first star of reciprocal lattice vectors for the respective commensurate structure.

angles, all commensurate structures are almost periodic repetitions of structures with  $r = 1$ .

In order to better understand the large angle commensurability effect, we have computed the interlayer local current measured from the bottom layer to the top layer in the  $1 \rightarrow 2$  setup. To that purpose, the bond current operator between a bottom layer site and a top layer site was evaluated at the energy  $\varepsilon = 0.225t$ . All the contributions that connect to a given site in the bottom layer were then added up and the obtained local interlayer current was assigned to that bottom layer site. The corresponding map is shown in Figs. 5(a-c) for three different commensurate angles [marked with an arrow in Fig. 4(b)]. Positive and negative values mean interlayer current flowing in and out of the given bottom layer site. The presence of a periodic pattern is apparent for the three angles, as can be seen in Figs. 5(a-c). We took the Fourier transform of the interlayer current by considering a rhombus with  $50 \times 50$  unit cells in the scattering region. The corresponding map is shown in Figs. 5(d-f), respectively for the three angles considered. The Fourier transform is extremely peaked, as inferred from the very small dark dots on a whitish background in Figs. 5(d-f). The peaks exactly fall onto the first star of reciprocal lattice vectors for the respective commensurate structure. Two representative vectors out of the six in the first star are indicated in each panel of Fig. 5(d-f). It follows that the observed periodicity for the interlayer current in Figs. 5(a-c) mimics the periodicity of the commensurate structure. The picture that emerges is that each Wigner-Seitz unit cell contributes roughly the same

to the interlayer current, so that a higher conductance is obtained for a higher number of Wigner-Seitz unit cells in the scattering region. Keeping the number of atoms in the scattering region roughly the same, commensurate angles with smaller Wigner-Seitz unit cells should have higher conductance, as observed.

### C. Intermediate twist angles

Figure 6(a) and 6(b) shows the conductance at three representative angles in the intermediate twist angle regime, respectively for the  $1 \rightarrow 1$  and  $1 \rightarrow 2$  setups and energies  $|\varepsilon| < 0.4t$ . A salient feature in this regime is the shoulder like behavior of the conductance around two particular energies roughly symmetric around zero. The behavior is more pronounced in the  $1 \rightarrow 1$  setup [Fig. 6(a)] which has a higher conductance, but it is clearly present in both setups. The energy scale associated with this feature correlates with the position of the two Van Hove singularities characteristic of tBLG at moderate twist angles. This is clearly seen with the help of Fig. 6(c), where the DOS of the system (scattering region) is shown for the three considered twist angles. The beginning of the shoulder-like feature just signals the strong suppression of the DOS after the Van Hove singularity. A similar effect is known to happen in single layer graphene after the Van Hove singularity [51], though at much higher energies.

The presence of Van Hove singularities in the DOS of tBLG for the moderate twist angle regime originates from saddle points in the energy dispersion. These saddle points are easily understood as a consequence of the hybridization between single layer Dirac cones [3, 5]. Due to rotation by the twist angle  $\theta$ , and considering for the moment uncoupled layers with  $t_{\perp} = 0$ , the single layer Dirac cones appear separated in reciprocal space by a distance  $\Delta K = 2K \sin(\frac{\theta}{2})$ , with  $K = 4\pi/(3\sqrt{3}a)$ . Turning on the interlayer coupling  $t_{\perp}$ , an avoided crossing at the energy scale  $\varepsilon = \pm \hbar v_f \Delta K/2$  gives rise to saddle points at the approximate energies

$$\varepsilon_{vh} \approx \pm \left( \hbar v_f \frac{\Delta K}{2} - \frac{t_{\perp}}{2} \right). \quad (6)$$

In Fig. 6 the vertical dashed lines are obtained through Eq. (6) for the three twist angles considered. The beginning of the shoulder-like feature in the conductance as we increase energy is very well captured by the energy scale  $\varepsilon_{vh}$ , as can be seen in Figs. 6(a-b).

### D. Small twist angles

It is in the small angle regime that most of the interesting novel phases have been found [1, 2, 9–20], associ-

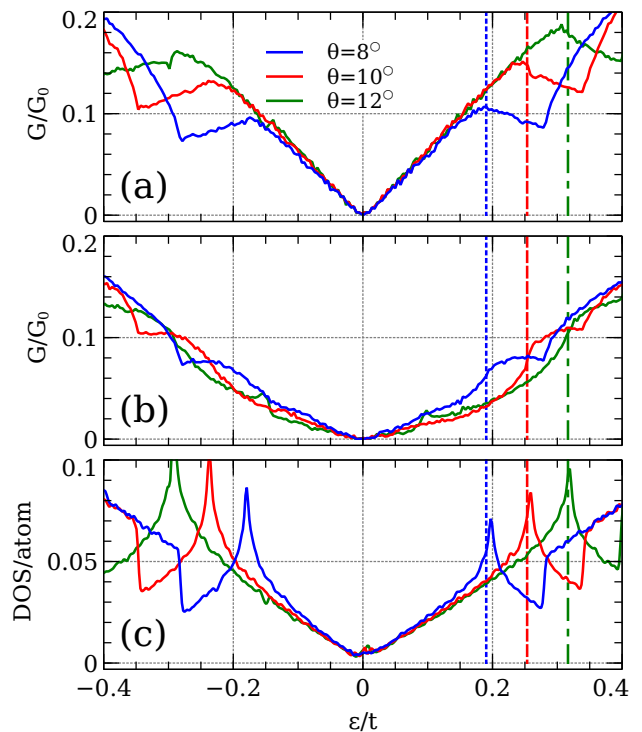


FIG. 6. Conductance,  $G$ , as a function of energy,  $\varepsilon$ , at three twist angles  $\theta = 8, 10, 12^\circ$ , for the  $1 \rightarrow 1$  (a) and  $1 \rightarrow 2$  (b) setups. The corresponding DOS is shown in (c). Vertical dashed lines depict the positions of Van Hove singularities computed through the approximate analytical expression given in Eq. (6) for the positive energy side.

ated to the presence of extremely narrow bands at low energies. Given the importance of transport measurements in accessing these phases, and the fact that the model we use here is considered a proper single particle description of tBLG, we address the question of what are the conductance characteristics for this model at low twist angles. The first result is that in the small angle regime  $1 \rightarrow 1$  and  $1 \rightarrow 2$  setups have very similar conductance at low energies. This is an indication that in this regime the scattering region is dominated by tBLG low energy properties, which weakens the differences between the two setups. This is to be expected whenever the scattering region is big enough to include a considerable number of moiré cells, as is the case for the angles we consider. In the following we show results only for the  $1 \rightarrow 1$  setup.

We start with incommensurate angles. In Fig. 7(a1-a3) the conductance at three representative small twist angles around the flat band regime is shown for energies  $|\varepsilon| \lesssim 0.04t$ . For the model considered in this work, the flat band regime occurs at  $\theta^* \approx 1.6^\circ$ , so that in Fig. 7(a1) the conductance is for an angle slightly below  $\theta^*$ , in Fig. 7(a2) very close to  $\theta^*$ , and in 7(a3) slightly above. To confirm that the scattering region is indeed displaying tBLG behavior around the flat band regime

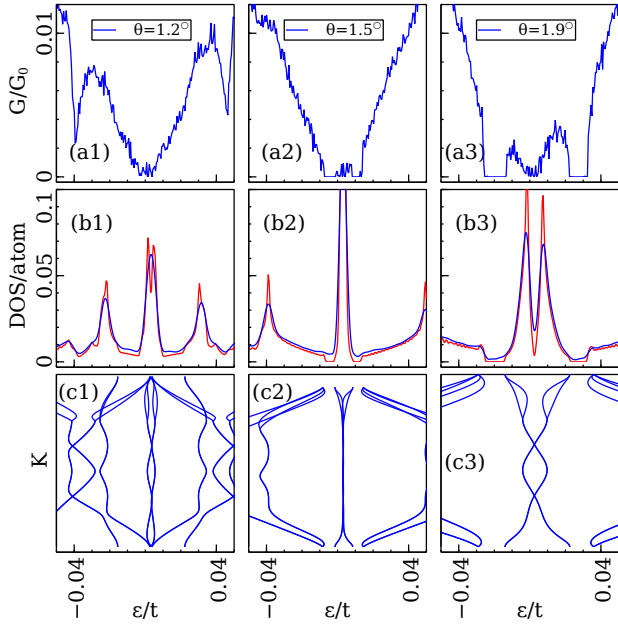


FIG. 7. (a1-a3) Conductance,  $G$ , as a function of energy,  $\varepsilon$ , at three incommensurate twist angles around the first *magic angle*  $\theta^* \approx 1.6^\circ$  for the  $1 \rightarrow 1$  setup. (b1-b3) DOS of the scattering region used in (a1-a3) is represented in blue. The DOS obtained using the plane wave expansion method is shown in red. (c1-c3) Band structure obtained by the plane wave expansion method.

we have calculated the DOS for the same angles, shown in Fig. 7(b1-b3) as blue curves, using the Kwant package [50]. The peaked DOS around zero energy, particularly for  $\theta \approx \theta^*$ , is a signature of tBLG behavior. Further confirmation comes from the DOS obtained with the plane wave expansion method [28], suitable for incommensurate structures [56, 57], shown as red curves in Fig. 7(b1-b3). The agreement is remarkable despite the fact that Kwant is a construction in real space using kernel polynomial methods while the plane wave expansion method works in reciprocal space. The plane wave expansion method allows also for the calculation of the band structure, which is displayed in Fig. 7(c1-c3). There, the appearance of very narrow bands at low energies, which become especially flat near  $\theta^*$ , is apparent.

The conductance in Figs. 7(a2) and 7(a3) has a low energy behavior which is not found at intermediate or large twist angles, nor in single or AB-stacked bilayer graphene [51]: low energy finite conductance flanked by transport gaps where the conductance vanishes. This is perfectly seen at  $\theta^*$  and when we approach  $\theta^*$  from above. Comparison with DOS and band structure, respectively in Figs. 7(b) and 7(c), shows that the transport gaps correlate perfectly with spectral gaps surrounding the low energy narrow bands. These transport gaps are in perfect agreement with those obtained experimentally when the low energy narrow bands are completely occupied,

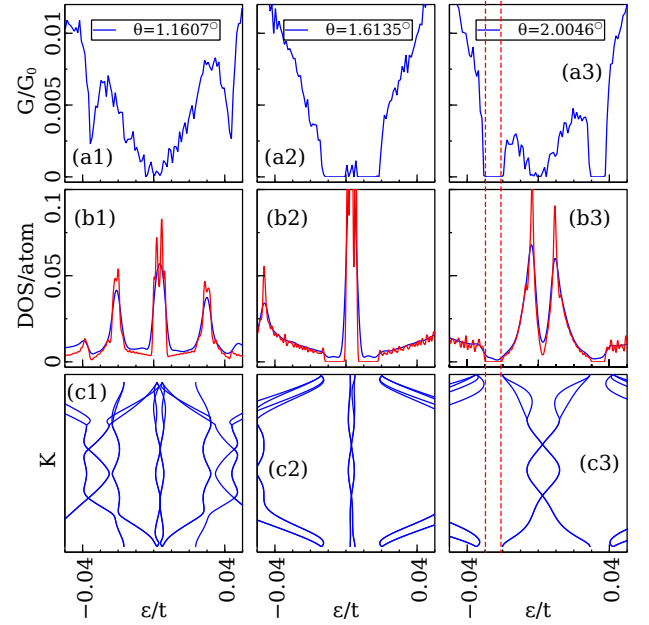


FIG. 8. (a1-a3) Conductance,  $G$ , as a function of energy,  $\varepsilon$ , at three commensurate twist angles around the first *magic angle*  $\theta^* \approx 1.6^\circ$  for the  $1 \rightarrow 1$  setup. The three structures are ( $m = 1, r = 1$ ) in terms of the integers  $m$  and  $r$  in Eq. (5). (b1-b3) DOS of the scattering region used in (a1-a3) is represented in blue. The DOS obtained using the diagonalization of the Bloch Hamiltonian is shown in red. (c1-c3) Band structure obtained by diagonalization of the Bloch Hamiltonian.

for a carrier density  $n = +n_s$ , or fully empty,  $n = -n_s$  [1, 2, 10, 11, 20, 39]. Note also the similarity between the inverted double-well-like conductance seen at low energies for  $\theta \simeq 2^\circ$  in Fig. 7(a3) and the measurements of Ref. [37] (compare with conductivity) and Refs. [9, 38] (compare with inverse resistance). This points to the conclusion that the observed behavior at small angles  $\theta \gtrsim \theta^*$  is still captured by the single particle description. Only very close to the *magic angle*  $\theta^*$  are correlation effects expected to become relevant. For angles  $\theta \lesssim \theta^*$ , as the one shown in Fig. 7(a1), the conductance still correlates well with the electronic structure. In particular, the two side peaks seen in the DOS of Fig. 7(b1) clearly match the beginning of a shoulder like feature in conductance as energy increases in absolute value. As can be appreciated in Fig. 7(c1), the low energy narrow bands are no longer well isolated from the other bands. This is the reason why there are no transport gaps in the conductance at low energy.

The results for commensurate angles are shown in Fig. 8. There is a close similarity with the results obtained for nearby commensurate angles, presented in Fig. 7. Commensurability effects, if present in the small twist angle regime, are significantly milder than at large angles. Note in particular how the transport gaps perfectly correlate with the spectrum, as is indicated by the

vertical lines on the right panels of Fig. 8. We note *en passant* that the DOS of the scattering region, shown in blue in Fig. 8(b), does not vanish in the energy region where transport gaps occur [this also happens for the incommensurate angles shown in Fig. 7]. However, by diagonalization of the Bloch Hamiltonian we obtain a vanishing DOS (in red) compatible the the spectral gap shown in Fig. 8(c). The reason is due to the open edges of the scattering region where localized states, which do not contribute to conductance, exist.

#### IV. CONCLUSIONS

We have characterized ballistic charge transport across a twisted bilayer graphene region connected to single-layer graphene leads. We analyzed two setups: a flake of graphene on top of an infinite graphene ribbon, dubbed  $1 \rightarrow 1$ , and two overlapping semi-infinite graphene ribbons, dubbed  $1 \rightarrow 2$ . As a function of twist angle, we found a strong dependence and identified three qualitatively different regimes. For large angles, there are pronounced fluctuations and strong commensurability effects: for generic incommensurate angles the two graphene layers effectively decouple yielding regions of high (low) conductance for the  $1 \rightarrow 1$  ( $1 \rightarrow 2$ ) geometry; large commensurate angles corresponding to a small Wigner-Seitz unit cell appear as sharp dips (peaks) in the conductance for the  $1 \rightarrow 1$  ( $1 \rightarrow 2$ ) case, for which the two layers are strongly coupled. For intermediate angles, we have found a correlation of the conductance features with the low energy Van Hove singularities of the DOS. This suggests that conductance measurements can be used as a measurement tool to determine the twist angle. Finally, for small angles, commensurate effects seem to be washed out. The almost flat bands appearing in this regime give rise to distinctive conductance features that correlate with those found in the DOS. In this regime, our results agree with the recent experimental findings where transport gaps have been correlated with spectral gaps [1, 2, 9–11, 20, 37–39].

HZO acknowledges the support from the DP-PMI and FCT-Portugal through scholarship PD/BD/113649/2015. B.A. acknowledges funding from the European Union’s Horizon 2020 research and innovation program under Grant Agreement No. 706538, and funding from FCT-Portugal through Grant No. CEECIND/02936/2017. EVC acknowledges support from FCT-Portugal through Grant No. UIDB/04650/2020. PR and HZO acknowledge support by FCT-Portugal through Grant No. UID/CTM/04540/2019. Some computations were performed on the Baltasar-Sete-Sóis cluster, supported by V. Cardoso’s H2020 ERC Consolidator Grant no. MaGRaTh-646597, computer assistance was provided by CENTRA/IST.

- 
- [1] Y. Cao, V. Fatemi, A. Demir, S. Fang, S. L. Tomarken, J. Y. Luo, J. D. Sanchez-Yamagishi, K. Watanabe, T. Taniguchi, E. Kaxiras, R. C. Ashoori, and P. Jarillo-Herrero, *Nature* **556**, 80 (2018), arXiv:1802.00553.
  - [2] Y. Cao, V. Fatemi, S. Fang, K. Watanabe, T. Taniguchi, E. Kaxiras, and P. Jarillo-Herrero, *Nature* **556**, 43 (2018), arXiv:1803.02342.
  - [3] J. M. B. Lopes dos Santos, N. M. R. Peres, and A. H. Castro Neto, *Phys. Rev. Lett.* **99**, 256802 (2007), arXiv:0704.2128.
  - [4] R. Bistritzer and A. H. MacDonald, *Proc. Natl. Acad. Sci.* **108**, 12233 (2011).
  - [5] J. M. B. Lopes dos Santos, N. M. R. Peres, and A. H. Castro Neto, *Phys. Rev. B* **86**, 155449 (2012), arXiv:1202.1088.
  - [6] G. De Trambly Laissardière, D. Mayou, and L. Magaud, *Nano Lett.* **10**, 804 (2010), arXiv:0904.1233.
  - [7] E. Suárez Morell, J. D. Correa, P. Vargas, M. Pacheco, and Z. Barticevic, *Phys. Rev. B* **82**, 121407 (2010), arXiv:1012.4320.
  - [8] S. Shallcross, S. Sharma, E. Kandelaki, and O. A. Pankratov, *Phys. Rev. B - Condens. Matter Mater. Phys.* **81**, 165105 (2010).
  - [9] T.-F. Chung, Y. Xu, and Y. P. Chen, *Phys. Rev. B* **98**, 035425 (2018).
  - [10] M. Yankowitz, S. Chen, H. Polshyn, Y. Zhang, K. Watanabe, T. Taniguchi, D. Graf, A. F. Young, and C. R. Dean, *Science* **363**, 1059 (2019).
  - [11] A. L. Sharpe, E. J. Fox, A. W. Barnard, J. Finney, K. Watanabe, T. Taniguchi, M. A. Kastner, and D. Goldhaber-Gordon, *Science* **365**, 605 (2019), arXiv:1901.03520.
  - [12] A. Kerelsky, L. J. McGilly, D. M. Kennes, L. Xian, M. Yankowitz, S. Chen, K. Watanabe, T. Taniguchi, J. Hone, C. Dean, A. Rubio, and A. N. Pasupathy, *Nature* **572**, 95 (2019), arXiv:1812.08776.
  - [13] Y. Choi, J. Kemmer, Y. Peng, A. Thomson, H. Arora, R. Polski, Y. Zhang, H. Ren, J. Alicea, G. Refael, F. von Oppen, K. Watanabe, T. Taniguchi, and S. Nadj-Perge, *Nat. Phys.* **15**, 1174 (2019), arXiv:1901.02997.
  - [14] Y. Jiang, X. Lai, K. Watanabe, T. Taniguchi, K. Haule, J. Mao, and E. Y. Andrei, *Nature* **573**, 91 (2019), arXiv:1904.10153.
  - [15] Y. Xie, B. Lian, B. Jäck, X. Liu, C.-L. Chiu, K. Watanabe, T. Taniguchi, B. A. Bernevig, and A. Yazdani, *Nature* **572**, 101 (2019), arXiv:1906.09274.
  - [16] S. L. Tomarken, Y. Cao, A. Demir, K. Watanabe, T. Taniguchi, P. Jarillo-Herrero, and R. C. Ashoori, *Phys. Rev. Lett.* **123**, 046601 (2019), arXiv:1903.10492.
  - [17] X. Lu, P. Stepanov, W. Yang, M. Xie, M. A. Aamir, I. Das, C. Urgell, K. Watanabe, T. Taniguchi, G. Zhang, A. Bachtold, A. H. MacDonald, and D. K. Efetov, *Nature* **574**, 653 (2019), arXiv:1903.06513.
  - [18] E. Codecido, Q. Wang, R. Koester, S. Che, H. Tian, R. Lv, S. Tran, K. Watanabe, T. Taniguchi, F. Zhang, M. Bockrath, and C. N. Lau, *Sci. Adv.* **5** (2019), 10.1126/sciadv.aaw9770, arXiv:1902.05151.
  - [19] H. Shi, Z. Zhan, Z. Qi, K. Huang, E. van Veen, J. Á. Silva-Guillén, R. Zhang, P. Li, K. Xie, H. Ji, M. I. Katsnelson, S. Yuan, S. Qin, and Z. Zhang,



- Nat. Commun. **11**, 371 (2020), arXiv:1905.04515.
- [20] M. Serlin, C. L. Tschirhart, H. Polshyn, Y. Zhang, J. Zhu, K. Watanabe, T. Taniguchi, L. Balents, and A. F. Young, *Science* **367**, 900 (2020), arXiv:1907.00261.
- [21] C. Shen, N. Li, S. Wang, Y. Zhao, J. Tang, J. Liu, J. Tian, Y. Chu, K. Watanabe, T. Taniguchi, R. Yang, Z. Y. Meng, D. Shi, and G. Zhang, (2019), arXiv:1903.06952.
- [22] X. Liu, Z. Hao, E. Khalaf, J. Y. Lee, K. Watanabe, T. Taniguchi, A. Vishwanath, and P. Kim, (2019), arXiv:1903.08130.
- [23] Y. Cao, D. Rodan-Legrain, O. Rubies-Bigorda, J. M. Park, K. Watanabe, T. Taniguchi, and P. Jarillo-Herrero, (2019), arXiv:1903.08596.
- [24] G. Chen, A. L. Sharpe, P. Gallagher, I. T. Rosen, E. J. Fox, L. Jiang, B. Lyu, H. Li, K. Watanabe, T. Taniguchi, J. Jung, Z. Shi, D. Goldhaber-Gordon, Y. Zhang, and F. Wang, *Nature* **572**, 215 (2019).
- [25] W.-J. Zuo, J.-B. Qiao, D.-L. Ma, L.-J. Yin, G. Sun, J.-Y. Zhang, L.-Y. Guan, and L. He, *Phys. Rev. B* **97**, 035440 (2018), arXiv:1711.08109.
- [26] F. Wu, T. Lovorn, E. Tutuc, I. Martin, and A. H. MacDonald, *Phys. Rev. Lett.* **122**, 086402 (2019).
- [27] L. Wang, E.-M. Shih, A. Ghiotto, L. Xian, D. A. Rhodes, C. Tan, M. Claassen, D. M. Kennes, Y. Bai, B. Kim, K. Watanabe, T. Taniguchi, X. Zhu, J. Hone, A. Rubio, A. Pasupathy, and C. R. Dean, (2019), arXiv:1910.12147.
- [28] C. Gonalo, B. Amorim, E. V. Castro, J. M. V. P. Lopes, and N. Peres, in *Handb. Graphene Vol. 3*, edited by M. Zhang (John Wiley & Sons, New Jersey, 2019) Chap. 6, pp. 177–230.
- [29] N. F. Q. Yuan, M. Koshino, L. Fu, T. Koretsune, M. Ochi, and K. Kuroki, *Phys. Rev. X* **8**, 031087 (2018).
- [30] L. Zou, H. C. Po, A. Vishwanath, and T. Senthil, *Phys. Rev. B* **98**, 085435 (2018), arXiv:1806.07873.
- [31] J. Kang and O. Vafek, *Phys. Rev. X* **8**, 031088 (2018).
- [32] H. C. Po, L. Zou, T. Senthil, and A. Vishwanath, *Phys. Rev. B* **99**, 195455 (2018), arXiv:1808.02482.
- [33] N. F. Q. Yuan and L. Fu, *Phys. Rev. B* **98**, 045103 (2018), arXiv:1803.09699.
- [34] S. Carr, S. Fang, H. C. Po, A. Vishwanath, and E. Kaxiras, *Phys. Rev. Res.* **1**, 033072 (2019), arXiv:1907.06282.
- [35] S. Shallcross, S. Sharma, and O. Pankratov, *Phys. Rev. B - Condens. Matter Mater. Phys.* **87**, 245403 (2013).
- [36] A. O. Sboychakov, A. L. Rakhmanov, A. V. Rozhkov, and F. Nori, *Phys. Rev. B* **92**, 075402 (2015).
- [37] Y. Cao, J. Y. Luo, V. Fatemi, S. Fang, J. D. Sanchez-Yamagishi, K. Watanabe, T. Taniguchi, E. Kaxiras, and P. Jarillo-Herrero, *Phys. Rev. Lett.* **117**, 116804 (2016), arXiv:1607.05147.
- [38] Y. Kim, P. Herlinger, P. Moon, M. Koshino, T. Taniguchi, K. Watanabe, and J. H. Smet, *Nano Lett.* **16**, 5053 (2016).
- [39] H. Polshyn, M. Yankowitz, S. Chen, Y. Zhang, K. Watanabe, T. Taniguchi, C. R. Dean, and A. F. Young, (2019), arXiv:1902.00763.
- [40] X. Liu, Z. Wang, K. Watanabe, T. Taniguchi, O. Vafek, and J. I. A. Li, (2020), arXiv:2003.11072.
- [41] H. Yoo, R. Engelke, S. Carr, S. Fang, K. Zhang, P. Cazeaux, S. H. Sung, R. Hovden, A. W. Tsien, T. Taniguchi, K. Watanabe, G.-C. Yi, M. Kim, M. Luskun, E. B. Tadmor, E. Kaxiras, and P. Kim, *Nat. Mater.* **18**, 448 (2019), arXiv:1804.03806.
- [42] M. Andelković, L. Covaci, and F. M. Peeters, *Phys. Rev. Mater.* **2**, 034004 (2018), arXiv:1705.05731.
- [43] E. H. Hwang and S. D. Sarma, (2019), arXiv:1907.02856.
- [44] F. Wu, E. Hwang, and S. Das Sarma, *Phys. Rev. B* **99**, 165112 (2019).
- [45] M. Pelc, E. S. Morell, L. Brey, and L. Chico, *J. Phys. Chem. C* **119**, 10076 (2015), arXiv:1407.6594.
- [46] D. A. Bahamon, G. G3mez-Santos, and T. Stauber, (2019), arXiv:1909.09341.
- [47] B. Padhi, A. Tiwari, T. Neupert, and S. Ryu, (2020), arXiv:2005.02406.
- [48] J. C. Slater and G. F. Koster, *Phys. Rev.* **94**, 1498 (1954), arXiv:1506.08190.
- [49] G. Trambly De Laissardi3re, D. Mayou, and L. Magaud, *Phys. Rev. B - Condens. Matter Mater. Phys.* **86**, 125413 (2012).
- [50] C. W. Groth, M. Wimmer, A. R. Akhmerov, and X. Waintal, *New J. Phys.* **16**, 063065 (2014), arXiv:1309.2926.
- [51] H. Z. Olyaei, P. Ribeiro, and E. V. Castro, *Phys. Rev. B* **99**, 205436 (2019), arXiv:1810.11743.
- [52] E. Su3rez Morell, P. Vargas, L. Chico, and L. Brey, *Phys. Rev. B - Condens. Matter Mater. Phys.* **84**, 195421 (2011), arXiv:1112.5467.
- [53] M. N. van der Linden, J. P. K. Doye, and A. A. Louis, *J. Chem. Phys.* **136**, 54904 (2012).
- [54] P. Moon, M. Koshino, and Y. W. Son, *Phys. Rev. B* **99**, 165430 (2019).
- [55] R. Bistritzer and A. H. MacDonald, *Phys. Rev. B* **81**, 245412 (2010), arXiv:1002.2983.
- [56] B. Amorim, *Phys. Rev. B* **97**, 165414 (2018), arXiv:1711.02499.
- [57] B. Amorim and E. V. Castro, (2018), arXiv:1807.11909.